Published in final edited form as:
J Inorg Biochem. 2009 January ; 103(1): 10–19. doi:10.1016/j.jinorgbio.2008.08.012.

^{1}H NMR study of the effect of variable ligand on heme oxygenase electronic and molecular structure

Li-Hua Ma[a], **Yangzhong Liu**[a,1], **Xuhong Zhang**[b], **Tadashi Yoshida**[b], and **Gerd N. La Mar**[a,*]
[a]Department of Chemistry, University of California, Davis, CA 95616, United States
[b]Department of Biochemistry, Yamagata University School of Medicine, Yamagata 990-9585, Japan

Abstract

Heme oxygenase carries out stereospecific catabolism of protohemin to yield iron, CO and biliverdin. Instability of the physiological oxy complex has necessitated the use of model ligands, of which cyanide and azide are amenable to solution NMR characterization. Since cyanide and azide are contrasting models for bound oxygen, it is of interest to characterize differences in their molecular and/or electronic structures. We report on detailed 2D NMR comparison of the azide and cyanide substrate complexes of heme oxygenase from *Neisseria meningitidis*, which reveals significant and widespread differences in chemical shifts between the two complexes. To differentiate molecular from electronic structural changes between the two complexes, the anisotropy and orientation of the paramagnetic susceptibility tensor were determined for the azide complex for comparison with those for the cyanide complex. Comparison of the predicted and observed dipolar shifts reveals that shift differences are strongly dominated by differences in electronic structure and do not provide any evidence for detectable differences in molecular structure or hydrogen bonding except in the immediate vicinity of the distal ligand. The readily cleaved C-terminus interacts with the active site and saturation-transfer allows difficult heme assignments in the high-spin aquo complex.

Keywords

Neisseria meningitidis heme oxygenase; Azide complex; Magnetic anisotropies; Dipolar shifts; H-bonding

1. Introduction

Heme oxygenase [1], HO, a member of a class of non-metal enzymes that utilize hemin as cofactor and substrate to convert it into iron, CO and biliverdin via the intermediates, *meso*-hydroxyhemin, verdoheme and iron-biliverdin [2–6]. HOs are widely distributed and have been characterized in detail for mammals, plants, cyanobacteria and some pathogenic bacteria. The current understanding of the structure/function relationships for HOs has been aided significantly by crystallographic and NMR spectroscopic structural characterization of primarily human, hHO [7–12] and rat HO [13–17], and on the HOs from the pathogenic bacteria *Neisseria meningitidis*, *Nm*HO [18–26], *Corynebacterium diphtheriae*, *Cd*HO [16,17,27,28], and *Pseudomonas aeruginosa*, *Pa*HO [25,29–32]. The diverse HOs exhibit a remarkably conserved fold, in spite of only limited sequence homology, that consists of primarily α-helices where the substrate binds to a conserved His near the enzyme surface. Moreover, each HO

*Corresponding author. Tel.: +1 530 752 0958; fax: +1 530 752 8995. *E-mail address:* lamar@chem.ucdavis.edu (G.N. La Mar).
[1]Present address: School of Chemistry and Material Science, University of Science and Technology, Hefei 230026, PR China.

possesses several ordered water molecules in the distal pocket that are implicated in the HO mechanism [4–6,33]. The stereoselectivity of the reaction(only α-meso cleavage in mammalian HOs) is rationalized by steric blocking by the distal helix of three meso positions and steric tilt/orientation of the activated Fe^{+3}–OOH towards the fourth unblocked meso position. The stability of Fe^{+3}–OOH to O–O cleavage to yield inactive ferryl species common to peroxidases and cytochromes P450 has been linked to the novel interaction of the exogenous ligand with primarily ordered water molecules [7,8,13–15,18,19,27,29]. Solution ^{1}H NMR has shown [9, 10,20,23,25,34,35] that HOs possess an extended distal H-bond network that contains some much stronger-than normal H-bonds and that several of the ordered water molecules are imbedded within this H-bond network. The fact that mutagenesis of the same key residue within this network of HOs [36–38] with highly homologous distal pocket structures differentially effects product formation, suggest that an improved understanding of the influence of the nature of the exogenous ligand on the H-bond network is desirable.

The only readily NMR-addressable, physiologically relevant HO species are diamagnetic, substrate-free, apo-HO, and the resting-state, high-spin ferric, substrate aquo complex. However, while the information content of the high-spin aquo complex is very rich [21,35, 39], strong paramagnetic relaxation severely hampers resonance assignment in the absence of isotope-labeled substrate. Since both the initial ferrous-O_2 (with one exception [27]) and activated ferric-hydroperoxy [33] species are generally too unstable to investigate at ambient temperatures, both crystal and solution characterization have been carried out on numerous physiologically non-relevant derivatives which model various aspects of HO species. Thus the ferric cyanide [9,14,21,30,34] or azide [13,25] and ferrous NO [8,19,40] or CO [40] complexes have served as models for the oxy complex, and the ferric hydroxy complex has been proposed [5,31] to mimic the hydroperoxy species. For the purposes of NMR spectroscopy, the low-spin azide and cyanide complexes of ferri-hemoproteins are most readily characterized due to favorable relaxation properties that allow detailed 2D NMR characterization, large magnetic anisotropy that facilitates signal resolution, and relatively simple but robust interpretive bases for the hyperfine shifts in terms of functionally relevant molecular/electronic structural parameters [39].

Our interests here focus on the azide complex of protohemin, PH, bound to *Nm*HO for three main reasons. The first is the anticipated set of favorable circumstances that would allow conveniently attainable substrate resonance assignments in the azido-complex to be extended, via magnetization-transfer [41], to the much more difficult-to-assign high-spin, ferric-aquo complexes [25,26,32,39,42,43]. Second, azide provides an oxy model that contrasts cyanide in several ways. Thus, cyanide, like O_2, is diatomic but prefers to bind linear and normal to the heme (while the FeOO bond is bent), and is a much weaker H-bond acceptor than O_2. Azide exhibits the bent structure like O_2, and its H-bond acceptor strength lies between that of O_2 and cyanide. Hence, it is of interest to characterize any differences in molecular structure and/ or H-bond strength in the H-bond network between the azide and the previously characterized [20] cyanide complex of *Nm*HO. Third, the structural and functional properties of *Nm*HO are, for the most part, typical of those of the structurally characterized mammalian and other bacterial HOs [2–5,7,8,13,18,19,27,29,44]. However, a C-terminal tripeptide His207Arg208His209 of *Nm*HO, found “missing” in the crystal structures [18,19] and attributed to disorder, was found ordered in solution for *Nm*HO–PH–CN [20,35] and shown to interact strongly with the substrate pocket. Moreover, this C-terminal Arg208His209 peptide is spontaneously cleaved in solution [20,35], which suggests the possibility that the C-terminus was also cleaved in the crystal. The “loss” of this C-terminal dipeptide by “aging” leads to an increased rate of product biliver-din release [35], implicating the C-terminal tail in modulating *Nm*HO activity. It is of interest to ascertain whether the C-terminus similarly interacts with the active site and cleaves in the azide as found for the cyanide complex [35].

Changes in molecular structure upon ligand binding in diamagnetic enzymes are readily detected in the perturbation of chemical shifts of the ^{15}N and ^{1}H in [^{1}H–15N]-HSQC spectra [45]. However, changes in chemical shifts with ligands in paramagnetic enzymes do not allow the same confident analysis due to the presence of dipolar shifts, δ_{dip}, given by [39,46–48]

$$\delta_{dip} = (24\pi\mu_0 N_A)^{-1}[3\Delta\chi_{ax}(3\cos^2\theta' - 1)R^{-3} + 2\Delta\chi_{rh}(\sin^2\theta' \times \cos 2\Omega')R^{-3}]\Gamma(\alpha,\beta,\gamma), \quad (1)$$

where $\Delta\chi_{ax}$ and $\Delta\chi_{rh}$ are the axial and rhombic anisotropies of the diagonal paramagnetic susceptibility tensor, χ, R, θ', Ω' define the nucleus in an iron-centered, reference coordinate system, x', y', z' (Fig. 1), and $\Gamma(\alpha,\beta,\gamma)$ is the Euler rotation that converts the reference into the magnetic coordinate system, x, y, z, in which χ is diagonal. Since the dipolar shifts are very long-ranged, nuclei up to 25 Å from the iron in low-spin ferrihemoproteins can experience non-negligible δ_{dip} whose magnitude can depend on the detailed electronic structure of the iron-center ($\Delta\chi_{ax}$, $\Delta\chi_{rh}$, α, β, γ in Eq. (1)), even if the molecular structure (i.e., R', θ', Ω' in Eq. (1)) is strongly conserved. Both the anisotropy and orientation of χ can be determined if a significant portion of the active site residues are assigned and their dipolar shifts quantitated.

To date, only the substrate resonances have been assigned for *Nm*HO–PH–N_3 [25], although both substrate and residue backbone assignments have been reported for *Pa*HO–PH–N_3 [32]. It was noted that the pattern of PH methyl hyperfine shifts in the *Pa*HO azide complex differed from that of the same cyanide complex, and the novel intermediate-spin, $S = 3/2$ ground state, was proposed [25] to account for this. We report here on the detailed assignments of the active site of *Nm*HO–PH–N_3, and determine the magnetic axes which indicate that, although significant differences in chemical shifts are observed between the azide and cyanide complexes, they are consistent with arising primarily from differences in the electronic structure of the chromophore and not in the molecular structure and H-bond strengths. Moreover, the C-terminus interacts with the active site and is cleaved in a manner very similar to that reported for the cyanide and aquo complexes [22,24]. Lastly, we show that the azide complex does provide a ready access to the elusive assignment of the substrate resonances in resting-state HO complexes [21,35,39].

2. Materials and methods

2.1. Sample preparation

The apo-*Nm*HO samples used in this study are the same as described in detail previously [20]. Stoichiometric amounts of protohemin, PH (Fig. 1), dissolved in 0.1 M KOH in $^{1}H_2O$, were added to apo-*Nm*HO in phosphate buffer (50 mM, pH 7.0). The substrate complex was purified by column chromatography on Sephadex G25, and phosphate-buffered KN_3 solution at pH 7.1 was titrated in until >95% conversion to the *Nm*HO–PH–N_3 complex was achieved ($[N_3^-]$~50 mM). Samples in $^{1}H_2O$ were converted to $^{2}H_2O$ by column chromatography [49].

2.2. NMR spectroscopy

^{1}H NMR data were collected on Bruker AVANCE 500 and 600 spectrometers operating at 500 and 600 MHz, respectively. Reference spectra were collected in $^{1}H_2O$ and $^{2}H_2O$ over the temperature range 15–35 °C at both a repetition rate of 1 s^{-1} over 40 ppm spectral width and at 5 s^{-1} over a 200 ppm spectral width. Steady-state magnetization-transfer [41] (NOE or exchange) difference spectra were generated from spectra with on-resonance, and off-resonance, saturation of the desired signals; to detect exchange with H_2O, selective 3:9:19 excitation [50] was used. Chemical shifts are referenced to 2,2-dimethyl-2-silapentane-5-sulfonate (DSS) through the water resonance calibrated at each temperature. Non-selective

T_1s were determined by the standard inversion-recovery pulse sequence and estimated from the null point. 600 MHz NOESY spectra [51] (mixing time 40 ms; repetition rate 1–2 s^{-1}) and 500 MHz Clean-TOCSY spectra (to suppress ROESY response [52]; 25°, 35°C, spin lock 25 ms; repetition rate 1–2 s^{-1}) were recorded over a bandwidth of 25 KHz (NOESY) and 12 KHz (TOCSY) using 512 t1 blocks of 128 and 256 scans each consisting of 2048 t2 points. 2D data sets were processed using Bruker XWIN software on a Silicon Graphics Indigo workstation. The processing consisted of 30°- or 45°-sine-squared-bell-apodization in both dimensions, and zero-filling to 2048 × 2048 data points prior Fourier transformation.

2.3. Magnetic axes determination

The anisotropy and orientation of χ were determined [20,23,39,47,48] by finding the Euler rotation angles, Γ(α,β,γ), that rotate the crystal structure based, iron-centered reference coordinate system, *x′*, *y′*, *z′*, into the magnetic coordinate system, *x*, *y*, *z*, where the paramagnetic susceptibility tensor, χ, is diagonal; α, β and γ are the three Euler angles where β corresponds to the tilt of the major magnetic axis, *z*, from the heme normal *z′*, α reflects the direction of this tilt, and is defined as the angle between the projection of the *z* axis on the heme plane and the *x′* axis (Fig. 1), and κ = α + γ is the angle between the projection of the *x*, *y* axes onto the heme plane and locates the rhombic axes. A least-square search was carried out for the minimum in the error function [39,47,48], *F*/*n*

$$F/n\sum_{i=1}^{n}\left|\delta_{\mathrm{dip}}(\mathrm{obs})-\delta_{\mathrm{dip}}(\mathrm{calc})\right|^2, \tag{2}$$

with observed dipolar shift, δ_{dip}(obs) given by

$$\delta_{\mathrm{dip}}(\mathrm{obs})=\delta_{\mathrm{DSS}}(\mathrm{obs})-\delta_{\mathrm{DSS}}(\mathrm{dia}), \tag{3}$$

where δ_{DSS}(obs) and δ_{DSS}(dia) are the chemical shifts, in ppm, referenced to DSS, for the paramagnetic *Nm*HO–PH–N_3 complex and an isostructural diamagnetic complex, respectively. In the absence of an experimental δ_{DSS}(dia) for the latter, it may be reasonably estimated by the ShiftX program [53] based on molecular structure, [19] as described previously for *Nm*HO–PH–CN [20,21,24] and *Nm*HO–PH–H_2O [21,23]. Error analyses were performed with Levenberg–Marguard method, [54,55] as described previously [56]. The ShiftX program has been shown [53] to provide reliable estimates to within one- or two-tenth of a ppm with random deviations. Since numerous protons for *Nm*HO–PH–N_3 exhibit $|\delta_{dip}|$ in the range 2–3 ppm, the potential error in δ_{dip}(obs) becomes negligible. An uncertainty of ~0.1 ppm for δ_{dip}(calc) dictates that only differences in chemical shifts between two complexes greater than 0.2 ppm can be considered significant.

3. Results

3.1. Comparison of azide and cyanide complexes

The resolved portions of the 600 MHz ^{1}H NMR spectrum of native *Nm*HO–PH–N_3 in ^1H_2O (Fig. 2A); and ^2H_2O (Fig. 2B) reveal the assigned [25] three low-field heme methyl peaks in the 18–22 ppm window, and a strongly shifted and strongly relaxed labile proton signal at 32 ppm, as well as two methyls and several single protons in the upfield spectral window. Protohemin peaks are labeled by the Fischer notation and residue peaks by residue number for peptide NHs, and both residue number and position for other proton signals. The minor methyl peaks in the 19–21 ppm window, labeled with asterisks (in Fig. 2A and B), arise from a minor species. The resolved heme methyls of native *Nm*HO–PH–N_3 exhibit nonselective T_1s of ~40

ms, and the upfield vinyl H_β display T_1 ~ 60 and 80 ms, while the upfield peaks labeled 26γ1 and 119β1 exhibit T_1s ~ 50 and ~40 ms. The low-field labile proton peak labeled 121 exhibits a T_1 ~ 30 ms. The same spectral regions of *Nm*HO–PH–CN in ^1H_2O, with the reported assignments, [20] are reproduced in Fig. 2A′. The temperature dependence for the azide complex (not shown; see Supporting Information) reveals weak anti-Curie behavior for the PH methyls and His23 $N_\delta H$ and Curie behavior for other protons.

3.2. Cross-saturation between NmHO–PH–H_2O and NmHO–PH–N_3

Fig. 3 illustrates the heme methyl spectral window for the high-spin [21] *Nm*HO–PH–H_2O (Fig. 3A and B) and *Nm*HO–PH–N_3 complexes (Fig. 3A′ and B′) for an equilibrium mixture of *Nm*HO–PH–H_2O/*Nm*HO–PH–N_3 shortly after preparation (Fig. 3A and A′) and ~24 h later (Fig. 3B and B′). The *Nm*HO–PH–H_2O methyl peaks in Fig. 3A and B illustrate the spontaneous conversion of the WT (designated A; Ser2-His209, peak $i\mathrm{CH}_3^{\mathrm{A}}$) $Nm\mathrm{HO}^{\mathrm{A}}$–PH–$H_2O$, to the cleaved [22] (designated X; Ser2-Arg207, peak $i\mathrm{CH}_3^{\mathrm{x}}$), $Nm\mathrm{HO}^{\mathrm{X}}$–PH–$H_2O$, complexes (Fig. 3A and B), as detailed previously [20,22]. Only the $8\mathrm{CH}_3^{\mathrm{A}}$, $8\mathrm{CH}_3^{\mathrm{X}}$ chemical shifts can be distinguished [22] in the high-spin complex. The conversion of A→X for the aquo complexes (Fig. 3A and B), is also observed for the azide complex (Fig. 3A′ and B′).

The panels C–G of Fig. 3 illustrate the magnetization-transfer [41] observed for the azide complex (Fig. 3C′–G′), as the assigned methyls [21] of the aquo complex (Fig. 3C–G) are saturated, as indicated by vertical arrows. Saturating the $8\mathrm{CH}_3^{\mathrm{A}}$ peak of $Nm\mathrm{HO}^{\mathrm{A}}$–PH–$H_2O$ confirms the previously reported [25] $8\mathrm{CH}_3^{\mathrm{A}}$ peak of $Nm\mathrm{HO}^{\mathrm{A}}$–PH–$N_3$ (Fig. 3D and D′) and saturation of $8\mathrm{CH}_3^{\mathrm{X}}$ of $Nm\mathrm{HO}^{\mathrm{X}}$–PH–$H_2O$ identifies $8\mathrm{CH}_3^{\mathrm{X}}$ for $Nm\mathrm{HO}^{\mathrm{X}}$–PH–$N_3$. Similarly, saturation of the A/X pairwise degenerate $5\mathrm{CH}_3^{\mathrm{A}}/5\mathrm{CH}_3^{\mathrm{X}}$,$1\mathrm{CH}_3^{\mathrm{A}}/1\mathrm{CH}_3^{\mathrm{X}}$ and $3\mathrm{CH}_3^{\mathrm{A}}/3\mathrm{CH}_3^{\mathrm{X}}$ peaks (Fig. 3E–G), respectively, leads to cross-saturation to the previously assigned [25] $i\mathrm{CH}_3^{\mathrm{A}}$ for i = 1, 3, 5 of the $Nm\mathrm{HO}^{\mathrm{A}}$–PH–$N_3$/*Nm*HO–PH–$N_3$, which confirms the methyl assignment for the WT–A complex [25] and locates the same $i\mathrm{CH}_3^{\mathrm{x}}$ peak for $Nm\mathrm{HO}^{\mathrm{X}}$–PH–$N_3$ (Fig. 3E′–G′, respectively). The magnitude of the cross-saturation in a steady-state difference spectrum for *Nm*HO–PH–H_2O/*Nm*HO–PH–N_3 is very similar to that observed in the pair metMbH_2O/metMbN_3 [43]. The majority of the remaining 2D NMR characterization was carried out on the uncleaved, native *Nm*HO–PH–N_3 complex. The absence of a superscript hereafter designates the “A” or WT complex. The chemical shift for the assigned protohemin peaks are very similar to that reported previously [25] and is listed in Supplementary material (Table S1).

3.3. Residue assignment protocols

The assignment protocols for the *Nm*HO–PH–N_3 complex are the same as those previously successfully [20,24] employed for the *Nm*HO–PH–CN complex; sequential assignments by the helical $N_i - N_{i+1}$, α_i-N_{i+1}, β_i-N_{i+1}, α_i-N_{i+3} and/or α_i–β_{i+3}, NOESY connections among TOCSY-identified spin systems [57], when allowed by resolution and relaxation. Since relaxation is ~5-fold faster in N_3^- than CN^- complexes, [20] paramagnetic relaxation ($T_1 \propto R^{-6}$) and NOESY data are used to support assignments when line broadening obliterates TOCSY cross-peaks. Extensive use is made of 2D data at several temperatures to establish the uniqueness of cross-peaks. The assignments are greatly facilitated by the fact that the pattern of dipolar-shifted, non-ligated amino acid residue resonances in *Nm*HO–PH–N_3 is very similar to that for the *Nm*HO–PH–CN complex [20]. This is obvious even in the reference spectra (Fig. 2), as shown for the low-field Ala121 NH and the upfield Ala26 and Leu119 methyls shifts. Hence, we illustrate 2D data only for assigning the key proximal helix residues in *Nm*HO–PH–

N_3 necessary to determine the magnetic axes and to identify key heme contact residues. Other 2D data are provided in Supplementary material (Table S2).

3.4. The proximal helix

Sequential α-helical contacts (illustrated in Fig. 4) among TOCSY-detected residues (not shown; see Supplementary material; Figs. S1 and S2) locate the fragment: AMX_i-Thr_{i+1}-Thr_{i+2}-Ala_{i+3}-Val_{i+4}-N_{i+5}-AMX_{i+6}-N_{i+7}-Val_{i+8}, which must arise from the proximal helix residues Asp18-Val26. The key axial His23 $C_\alpha H–C_\beta H_2$ fragment is too strongly relaxed to exhibit TOCSY cross-peaks (or NOESY cross-peaks in Fig. 4) to N_{i+5}, but the characteristic NOESY intra-residue cross-peaks among the strongly relaxed and strongly low-field shifted protons are readily observed under more rapid pulsing conditions (not shown; see Supplementary material; Fig. S3). NOESY connections of residues with PH are shown in Fig. 5. The obvious Val26 with its expected methyl NOESY cross to the $3CH_3$ (Fig. 5D) and $4H_\beta$s (Fig. 5E) exhibits TOCSY connections for only a $C_\alpha H–C_\beta H–C_\gamma H_3$ fragment, but the expected, and observed, resolved and relaxed (T_1 ~ 50 ms) $C_{\gamma 2}H_3$ peak exhibits the expected intra- and inter-residue NOESY cross-peak. The very strongly relaxed (<20 ms at low temperature) labile proton at 32 ppm exhibits significant saturation-transfer above 20 °C, and displays no NOESY cross-peaks. Both the relaxation and saturation-transfer are those expected for the His23 ring $N_\delta H$, as confirmed directly [20] in *Nm*HO–PH–CN. The chemical shifts for the proximal helix residues for *Nm*HO–PH–N_3 are listed in Table 1, where they can be compared to those previously reported for the *Nm*HO–PH–CN complex; [20] the similarity in both the pattern of shift and the shift magnitudes is striking.

3.5. The distal helix

A three-residue helical fragment Phe_i-X_{i+1}-Phe_{i+2} are observed (not shown) which is unique to Phe123-Leu124-Phe125 of the distal helix. The distal helix is sufficiently close to the iron that the factor ~4–5 increased relaxation rate in the azide compared to the cyanide complex [20] obliterates many TOCSY connections and interferes with even the NOESY detection of many $N_i + N_{i+1}$ contacts. The remainder of the distal helix is approached via multiple characteristic contacts to protohemin in the crystal structure [19] and *Nm*HO–PH–CN solution structure [20]. The contacts to substrate are illustrated in Fig. 5, with cross-peaks for $8CH_3$ (Fig. 5A) and $1CH_3$ (Fig. 5B) to Phe123 C_βHs and ring (not shown), $5CH_3$ to Cys113 ($C_\alpha H$; Fig. 5B), Gly116 (NH, $C_\alpha H$; Fig. 5B), Trp153 ring (Fig. 5B), and Tyr112 ring (not shown), and $7H_\alpha$ to Leu119 $C_\delta H_3$ (Fig. 5C). The identified Gly116 NH leads to both Glu115 and Ala114 via $N_i + N_{i+1}$ contacts (Fig. 4B). The TOCSY-detected $CH(CH_3)_2$ fragment in contact with the propionates H_βs (not shown) can only arise from Leu119. A pair of strongly relaxed, upfield shifted geminal protons with NOESY contact to both the Leu119 $C_\gamma H(C_\delta H_3)_2$ and a $C_\alpha H$, identify the Leu119 C_βHs, with the T_1 ~ 40 ms of the upfield peak consistent with an iron distance a little smaller than for a PH methyl. The expected sequential $N_i - N_{i+1}$ connection for Ala114-Gly116 are illustrated in Fig. 4B. The strongly (Gly120) and moderately (Ala122) relaxed residues detected [20] in *Nm*HO–PH–CN could not be located; neither NH is predicted (not shown; see Supplementary material; Table S2) to be resolved in the azide complex. However, a strongly relaxed (T_1 ~ 30 ms; iron distance slightly shorter than for a PH methyl), low-field NH, exhibits the same pattern of NOESY cross-peaks [20] (and with approximately the same chemical shift), as Ala121 in *Nm*HO–PH–CN, and is so assigned. The 20 ms T_1 for the NH is consistent with iron distance slightly smaller than for heme methyl. The Phe45 ring makes the expected contacts to Val26 and Leu48 methyls (not shown; summarized in Fig. 1. The rings of Phe181 and Tyr184 were assigned based on the characteristic NOESY of a peak to $4H_\beta$s (Fig. 5E), $3CH_3$ and $4H_\beta$ (Fig. 5D and E). The pattern of observed (and expected) substrate contacts and inter-residue contacts are summarized in Fig. 1. The chemical shifts for distal helix residues are provided in Supplementary material (Table S2).

3.6. The distal H-bond network

Sequential $N_i - N_{i+1}$ connections locate the fragment Gly138-Ala143 (not shown; see Supplementary material (Fig. S4), with the same inter-residue connections observed in *Nm*HO–PH–CN, [20] with the peptide NHs of Arg140 and His141 exhibiting very strong low-field bias. Replacing ^1H_2O by ^2H_2O leads to exchange for many peptide NHs. However, numerous α-helical sequences ($N_i - N_{i+1}$) are clearly observed, even a month after solvent exchange, and the improved resolution allows the confirmation of the Ala114-Gly116 backbone connectivities, together with Ala114 contact to Phe52 and Glu115, and Glu115 contact with Trp153 (see Supplementary material; Fig. S5). Two other helical fragments are detected in ^2H_2O (not resolved in ^1H_2O), comprise Phe52-His53, and Ala180-Val187 (not shown; see Supplementary material; Fig. S5). The retention of the $N_i - N_{i+1}$ cross-peaks attest to remarkable slow exchange rates, as observed previously in *Nm*HO–PH–H_2O and *Nm*HO–PH–OH complexes [21,23]. The chemical shifts for these residues are listed in Supplementary material (Table S2), where they are compared to the data [20] for *Nm*HO–PH–CN.

3.7. The C-terminus

Crystal structures predict [18,19] only Gly120 $C_\alpha H$ (too strongly relaxed to be detected) and Phe123 $C_\beta Hs$ NOESY cross-peaks to $8CH_3$ (observed; [20] Fig. 5A). The contacts to the $8CH_3$ which are inconsistent with the crystal structures [7,8] are by the $C_\beta Hs$ (Fig. 5A) of a $C_\alpha HC_\beta H_2$ spin system that also makes contact to a narrow non-labile proton diagnostic of a His $C_\delta H$, and to a $C_\alpha H$ (Fig. 5A) of another residue in a fashion very similar to that reported for *Nm*HO–PH–CN [20,24]. The residues are similarly assigned to His207 and Arg208; chemical shifts are included in Supplementary material (Table S2). Qualitative modeling for *Nm*HO–PH–CN has indicated that the His207 peptide NH forms a H-bond with the carboxylate of Asp27 and the Arg208 guanidyl group makes a salt bridge with the 7-propionate. [22] Each of the His207/Arg208 NOESY cross-peaks moves upfield at lower temperatures (not shown), indicative of sizable upfield δ_{dip}. The observation of similar cross-peaks to $8CH_3$ in the azide and cyanide complexes dictates that the C-terminus interacts similarly with the substrate pocket in the two complexes. Consistent with this conclusion, the conversion of *Nm*HO–PH–N_3 from the native (A) to the cleaved (X) form, we observe (not shown) the loss of all His207 and Arg208 cross-peaks to the $8CH_3$.

3.8. Determination of the magnetic axes

The anisotropies and orientation of χ obtained from a five-parameter fit of δ_{dip}(obs) via Eqs. (1)–(3), using only non-labile proximal helix proton δ_{dip} as input, with geometric factors drawn from the *Nm*HO–PH–NO crystal structure [19], are: $\Delta\chi_{ax} = 2.3 \pm 0.1 \times 10^{-8}$ m^3/mol; $\Delta\chi_{rh} = -0.1 \pm 0.1 \times 10^{-8}$ m^3/mol, $\alpha = 240 \pm 20°$, $\beta = 5 \pm 1°$ and $\kappa \sim \alpha + \gamma = 140 \pm 30°$. The correlation between δ_{dip}(obs) and δ_{dip}(calc) for the optimized magnetic axes (closed markers) is excellent, as illustrated in Fig. 6. When δ_{dip}(obs) is plotted versus δ_{dip}(calc) for non-labile protons of residues not utilized in determining the magnetic axes (open markers in Fig. 6), a very good correlation is observed for all but the distal helix Ala121 residue. Leu119 has variable orientations in both crystals [18,19] and solution [20] and hence is not included. The reported [20] relevant parameters for *Nm*HO–PH–CN are $\Delta\chi_{ax} = 2.5 \pm 0.1 \times 10^{-8}$ m^3/mol, $\Delta\chi_{rh} = -0.6 \pm 0.1 \times 10^{-8}$ m^3/mol, $\alpha = 257 \pm 10°$, $\beta = 10 \pm 1°$ and $\kappa \sim \alpha + \gamma = 38 \pm 10°$ [20].

A large number of residues spread well over the enzyme exhibit significant δ_{dip}, as illustrated in a graph of δ_{dip}(calc) for peptide NHs as a function of sequence number as shown in Fig. 7A. The magnitude and distribution of δ_{dip}(calc) for the peptide NHs for the previously reported magnetic axes for *Nm*HO–PH–CN are also large and distributed similarly, but not identically, as illustrated in Fig. 7B. Thus, residues with $|\delta_{dip}| \geq 0.2$ ppm at 20 Åare common for both the azide and cyanide complexes, so that δ_{dip} for each of the complexes must be considered to

resolve any differences in molecular structure/H-bonding from differences in chromophore electronic/magnetic properties between the two complexes.

4. Discussion

4.1. Magnetic properties and electronic structure

The anisotropies and orientation of χ have been previously reported for *Nm*HO–PH–CN [20] and determined herein for *Nm*HO–PH–N_3. The $\Delta\chi_{ax}$ values are very similar, with that for the azide complex some 10% smaller than for the cyanide complex. The $\Delta\chi_{rh}$ is significantly smaller, and exhibits larger uncertainty, for the azide than cyanide complex. The tilt of the major magnetic (*z*-) axis is correlated [9,20,39] with the tilt of the Fe–N/C vector from the heme normal, is smaller in the azide than cyanide complex since the azide Fe–N_3 is bent (while the FeCN unit is linear) and experiences less steric tilting by the distal helix backbone. The Fe–N tilt in the azide complex is similar to that observed in the azide complex of rat HO [13]. In each case the tilt (−*z* direction) is towards the α-meso position that is cleaved. The magnetic properties are surprisingly similar in the azide and cyanide complexes in view of the proposed differences [25] in the spin state for the cyanide ($S = 1/2$) and azide ($S = 3/2$) complexes. This similarity in $\Delta\chi_{ax}$ values, however, does not preclude a difference in the spin state for the two ligands.

4.2. Comparison of molecular structure in the azide and cyanide complexes

The pattern of NOESY cross-peaks between the heme and contact residues and among residues in the presently studied azide complex, are very similar to those reported [20,22] for the *Nm*HO–PH–CN, which, in turn, were consistent with the *Nm*HO–PH prediction of the crystal structure [19], with the important exception of the $8CH_3$ contacts of the His207Arg208 C-terminus (see below)and the 180° rotation of the Gln49 and His53 side chain termini relative to those found in the crystal structures [18,19]. The NOESY contacts that differentiate the alternate orientation for Gln49 and His53 have been considered in detail previously [20,22, 24], and have been documented in all solution NMR studies.

Comparison of data for the azide and cyanide complexes of *Nm*HO–PH (Table 1; also see Supplementary material; Table S2) reveals that the chemical shifts for both non-labile and labile protons a large fraction of the residues differ significantly, even for some residues as far as 20 Å from the heme. The question that arises whether the widespread chemical shift differences between CN^- and N_3^- complexes of *Nm*HO–PH are due to primarily differences molecular structure/H-bonding or mainly different orientations/ anisotropies of χ (i.e., electronic structural properties of the chromophore)? The plot of δ_{dip}(calc) versus sequence number for the peptide NHs of *Nm*HO–PH–N_3 (Fig. 7A) and *Nm*HO–PH–CN (Fig. 7B) reveal large δ_{dip} with similar but not identical distribution about the enzyme manifold. Light is shed on this question by considering the differences in both the calculated dipolar shifts and observed shifts between the cyanide and azide complexes. Hence, we define the difference in the calculated dipolar shifts between the azide and cyanide complexes, $\Delta\chi_{dip}$(calc), as

$$\Delta\delta_{dip}(\text{calc}) = \delta_{dip}(\text{calc:NmHO} - \text{PH} - \text{N}_3) - \delta_{dip}(\text{calc:NmHO} - \text{PH} - \text{CH}), \quad (4)$$

and the difference in the observed shifts between the azide and cyanide complexes, $\Delta\chi_{DSS}$(obs), as

$$\Delta\delta_{DSS}(\text{obs}) = \delta_{DSS}(\text{obs:NmHO} - \text{PH} - \text{N}_3) - \delta_{DSS}(\text{obs:NmHO} - \text{Ph} - \text{CN}), \quad (5)$$

of which the latter is equal to $\Delta\chi_{dip}$(obs) in the absence of differences in molecular structure or H-bond strength.

We consider first the non-labile protons whose chemical shift differences could, in principle, reflect on molecular structural differences between the two complexes. The correlation between $\Delta\chi_{dip}$(calc), (Eq. (4)), versus $\Delta\chi_{DSS}$(obs), (Eq. (5)), for all assigned, non-labile protons for the two complexes, except Leu119 which exhibits variable orientations in both crystals [18,19] and solution, [20] is very good, as shown in Fig. 8, although there are some deviations in the magnitude of the difference for Ala121. However, this portion of the distal helix residue is very close to the exogenous ligand, and small, local structural accommodation of the distal helix not unexpected. Hence we conclude that the wide variation in chemical shift differences for non-labile protons between the azide and cyanide complex can be interpreted primarily on the basis of variable dipolar shifts, and that these shift differences provide no direct evidence for detectable molecular structural accommodation upon substituting N_3^- for CN^- as ligand in *Nm*HO, but do suggest some minor local structural accommodation of the distal helix near the exogenous ligand binding site.

4.3. Comparison of H-bonding in azide and cyanide complexes

The patterns of the peptide NH δ_{dip}(calc) with *Nm*HO residue number for *Nm*HO–PH–N_3 and *Nm*HO–PH–CN are plotted in Fig. 7A and B, respectively. Comparison of Fig. 7A and B reveals a very similar (but not identical) pattern of nodes (change in the sign of δ_{dip}(calc)) and similar magnitudes for δ_{dip}(calc). The differences between the two complexes are emphasized in Fig. 7C, where we plot $\Delta\chi_{dip}$(calc) (with ×8 vertical expansion relative to Fig. 7A and B) for the peptide NHs of the two complexes as given by Eq. (4), as a function of residue number. Fig. 7D provides the same plot of difference in observed peptide NH shifts between the azide and cyanide complexes, $\Delta\chi_{DSS}$(obs) (Eq (5)), which, in the absence of differences in H-bonding and molecular structure between the two complexes, should reflect the difference in δ_{dip}(obs). The very good correlation in both pattern and magnitude of the predicted difference in dipolar shifts and difference in observed shift argues strongly that, by far the primary source of the observed peptide NH chemical shift differences in the two complexes is the difference in the electronic structure, and not molecular structure and/or not H-bonding, between the N_3^- and CN^- complexes. The uncertainties in δ_{dip}(calc) for each complex preclude attributing any significance to chemical shift differences of less than ~0.2 ppm.

This conserved backbone NH H-bond strengths are consistent with the conclusion that molecular structure, as reflected in chemical shift for non-labile protons, differs inconsequentially between the azide and cyanide complex, except for the distal helix in the vicinity of the exogenous ligand. However, some local distortion of the distal helix portion near the exogenous ligand can be expected, and also observed for non-labile protons (Fig. 8).

The plot of $\Delta\delta_{dip}$(calc) versus $\Delta\delta_{DSS}$(obs) for side chain labile protons is included in Fig. 8 (crosses). Again, essentially all observed differences are accounted for by the predicted differences in δ_{dip}(calc), with the exception of the Gln49 $N_\varepsilon H$. The deviations in Fig. 8 corresponds to low-field bias for the N_3^- relative to the CN^- complex, reflecting a somewhat stronger Gln49 $N_\varepsilon H$ H-bonding in the former than the latter complex. The His53 $N_\varepsilon H$ exhibits a 0.13 ppm lower-field bias in the azide than cyanide complexes as predicted by Δδdip(calc). While this might suggest a slightly stronger H-bond in the azide complex, the difference is well under the 0.2 ppm uncertainty and may not be significant. The crystal structure of *Nm*HO–PH–NO shows[19] that Gln49 (rotated by 180°, as documented by solution NOESY cross-peaks [20,24]), is linked to the exogenous iron ligand by two ordered water molecules (#243 and #37), while His53 is linked to the same iron ligand by three water molecules (#77, #243 and #37). The low-field bias of the Gln49 NH in the N_3^- relative to the CN^- complex is

consistent with N_3^- serving as a slightly stronger H-bond acceptor than CN^-. The absence of any significant difference (>0.2 ppm) in the His53 $N_\varepsilon H$ shift in the two complexes likely reflects the weaker coupling to the axial ligand because of an additional intervening water molecule. Thus the available data provide direct evidence for a detectable difference in H-bond strength for only one residue in the distal H-bonding network.

4.4. Relationship to other studies

Magnetic axes have not been reported for either the CN^- or N_3^- complexes of *Pa*HO. However, *Pa*HO and *Nm*HO exhibit significant sequence and structural homology, [3,5,19,29,44] and backbone assignments have been reported for *Pa*HO–PH–CN and *Pa*HO– PH–N_3 complexes [32]. Widespread small to moderate chemical shift differences between the two complexes were interpreted as reflecting small conformational differences within a conserved secondary structure. [32] We note that the reported [32] patterns of shift differences (Fig. 8b in Ref. [32]) with residue number for peptide NHs and carboxyl $^{13}C{=}O$ in *Pa*HO–PH–N_3 and *Pa*HO–PH–CN complexes are very similar to that reported here (Fig. 7C) for the peptide NHs for the same pair of *Nm*HO–PH complexes. The more comprehensive backbone 3D NMR assignments of isotope-labeled *Pa*HO in both the paramagnetic azide and cyanide complexes [32], and more recently, in the ferrous CO complex [58] that can serve as a diamagnetic reference, provide the data necessary to quantitate the magnetic anisotropies/orientations and resolve differences in molecular structure/H-bonding from differences in electronic structure in the azide and cyanide complexes of *Pa*HO.

It has been reported that the dynamic stability, as evidenced by NH exchange [32] is significantly greater in the N_3^- than CN^- complexes of *Pa*HO, and preliminary data indicate moderately slower NH exchanges in azide than cyanide complexes of *Nm*HO. Such a difference in dynamic stability does not require any ground state molecular structural difference, only a shallower potential well for the CN^- complex [59]. Reduced dynamic stability of the CN^- complex can, in part, be rationalized by the strain induced in requiring a steric tilt of the Fe–CN unit [20], as also observed for the cyanide complex of rat HO [13].

4.5. Interaction of the C-terminus with the active site and cleavage Arg208His209

The initially prepared *Nm*HO–PH–N_3 complex exhibits essentially the same pattern of $8CH_3$ NOESY cross-peak as reported [20] for *Nm*HO–PH–CN, both of which are inconsistent with the crystal structures, [18,19] but consistent with an interaction of His207 and Arg208 with the active site as previously modeled [22] for the cyanide complex, where the Arg sidechain makes a salt bridge with the 7-propionate carboxylate, and the His207 peptide NH makes a H-bond to the carboxylate sidechain of Asp27 (see Fig. 9 of Ref. [22]). This interaction brings the His207 $C_\beta Hs$ and the Arg208 $C_\alpha H$ close to the $8CH_3$, as observed (Fig. 5A). The “aging” of the azide complex leads to the loss of the His207 and Arg208 $8CH_3$ contacts. The heme methyl resonances for the cleaved *Nm*HO–PH–N_3 complex have been observed in other NMR studies, [25] and the facile cleavage emphasizes the need to follow *Nm*HO studies by either NMR or mass spectrometry [24] to establish the integrity of the native *Nm*HO. Lastly, the electronic structure of the azide complex provides resolved substrate $1CH_3$ and $8CH_3$ signals for which it is much easier to detect and characterize the C-terminal interaction with the active site than in the cyanide complex, where the key heme methyl peaks are only partially resolved even in ^2H_2O solution. Further studies of the C-terminal interaction with substrates in azide complexes are in progress.

5. Conclusions

Several conclusions are indicated. (1) Saturation-transfer between the difficult-to-assign, strongly relaxed heme methyls of high-spin HO–PH–H_2O, and the more readily assigned heme

methyls of much less severely relaxed HO–PH–N_3, serves as a useful and effective route to identify the resonances in the physiologically relevant HO–PH–H_2O complex without reliance on isotope labeling. (2) Quantitative consideration of the anisotropies and orientations of χ in the CN^- and N_3^- complexes of *Nm*HO establishes that observed sizable and widespread chemical shift difference between the CN^- and N_3^- complex result primarily from the difference in the χ orientation/anisotropies. Therefore, no firm conclusions on differences in molecular structure and H-bond strengths for the two complexes can be drawn from the available NMR data; this conclusion may also apply to the same pair of *Pa*HO complexes [32]. (3) The crystallographically undetected [18,19] C-terminus interacts with the active site and the two terminal residues are spontaneously cleaved in the azide complex in a manner very similar to that reported for the cyanide complex [22,24].

It is important to note that, while the observed chemical shift differences between the azide and cyanide complexes of *Nm*HO–PH cannot be interpreted in terms of molecular structure/H-bond differences between the two complexes, this does not preclude the presence of some differences in molecular structure and H-bond strength. This is due to the fact that the differences in δ_{dip}(-calc) are so large as to mask most differences in structure/H-bonding.

Supplementary Material

Refer to Web version on PubMed Central for supplementary material.

Abbreviations

HO, heme oxygenase; hHO, human heme oxygenase #1; *Nm*HO, *Neisseria meningitidis* heme oxygenase; *Cd*HO, *Corynebacterium diphtheriae* heme oxygenase; *Pa*HO, *Pseudomonas aeruginosa* heme oxygenase; NOE, nuclear Overhauser effect; NOESY, two-dimensional nuclear Overhauser spectroscopy; TOCSY, two-dimensional total correlation spectroscopy; PH, protohemin.

Acknowledgments

This work was supported by Grants from the National Institutes of Health, GM62830 (GNL), and HL16087 (GNL), and a Grant-in-Aid for Scientific Research (16570102) from the Ministry of Education and Sports, Science and Teaching, Japan (T.Y.).

Appendix

Appendix A. Supplementary material

Supplementary data associated with this article can be found, in the online version, at doi: 10.1016/j.jinorgbio.2008.08.012.

References

1. Tenhunen R, Marver HS, Schmid R. J. Biol. Chem 1969;244:6388–6394. [PubMed: 4390967]
2. Yoshida T, Migita CT. J. Inorg. Biochem 2000;82:33–41. [PubMed: 11132636]
3. Wilks A. Antioxid. Redox Sig 2002;4:603–614.
4. Ortiz de Montellano, PR.; Auclair, K. The Porphryin Handbook, Heme Oxygenase Structure and Mechanism vol. 12. Kadish, KM.; Smith, KM.; Guilard, R., editors. San Diego, CA: Elsevier Science; 2003. p. 175-202.
5. Rivera M, Zeng Y. J. Inorg. Biochem 2005;99:337–354. [PubMed: 15598511]
6. Unno M, Matsui T, Ikeda-Saito M. Nat. Prod. Rep 2007;24:553–570. [PubMed: 17534530]

7. Schuller DJ, Wilks A, Ortiz de Montellano PR, Poulos TL. Nat. Struct. Biol 1999;6:860–867. [PubMed: 10467099]
8. Lad L, Wang J, Li H, Friedman J, Bhaskar B, Ortiz de Montellano PR, Poulos TL. J. Mol. Biol 2003;330:527–538. [PubMed: 12842469]
9. Li Y, Syvitski RT, Auclair K, Wilks A, Ortiz de Montellano PR, La Mar GN. J. Biol. Chem 2002;277:33018–33031. [PubMed: 12070167]
10. Li Y, Syvitski RT, Auclair K, Ortiz de Montellano PR, La Mar GN. J. Am. Chem. Soc 2003;125:13392–13403. [PubMed: 14583035]
11. Syvitski RT, Li Y, Auclair K, Ortiz de Montellano PR, La Mar GN. J. Am. Chem. Soc 2002;124:14296–14297. [PubMed: 12452690]
12. Ogura H, Evans JP, Ortiz de Montellano PR, La Mar GN. Biochemistry 2008;47:421–430. [PubMed: 18078349]
13. Sugishima M, Sakamoto H, Higashimoto Y, Omata Y, Hayashi S, Noguchi M, Fukuyama K. J. Biol. Chem 2002:45086–45090. [PubMed: 12235152]
14. Sugishima M, Sakamoto H, Higashimoto Y, Noguchi M, Fukuyama K. J. Biol. Chem 2003;278:32352–32358. [PubMed: 12794075]
15. Sugishima M, Migita CT, Zhang X, Yoshida T, Fukuyama K. Eur. J. Biochem 2004;271:4517–4525. [PubMed: 15560792]
16. Li Y, Syvitski RT, Auclair K, Ortiz de Montellano PR, La Mar GN. J. Biol. Chem 2003;279:10195–10205. [PubMed: 14660632]
17. Chu GC, Tomita T, Sönnichsen FD, Yoshida T, Ikeda-Saito M. J. Biol. Chem 1999;274:24490–24496. [PubMed: 10455111]
18. Schuller DJ, Zhu W, Stojiljkovic I, Wilks A, Poulos TL. Biochemistry 2001;40:11552–11558. [PubMed: 11560504]
19. Friedman JM, Lad L, Deshmukh R, Li HY, Wilks A, Poulos TL. J. Biol. Chem 2003;278:34654–34659. [PubMed: 12819228]
20. Liu Y, Zhang X, Yoshida T, La Mar GN. Biochemistry 2004;43:10112–10126. [PubMed: 15287739]
21. Liu Y, Zhang X, Yoshida T, La Mar GN. J. Am. Chem. Soc 2005;127:6409–6422. [PubMed: 15853349]
22. Liu Y, Ma L-H, Satterlee JD, Zhang X, Yoshida T, La Mar GN. Biochemistry 2006;45:3875–3886. [PubMed: 16548515]
23. Ma L-H, Liu Y, Zhang X, Yoshida T, La Mar GN. J. Am. Chem. Soc 2006;128:6657–6668. [PubMed: 16704267]
24. Liu Y, Ma L-H, Zhang X, Yoshida T, Satterlee JD, La Mar GN. Biochemistry 2006;45:13875–13888. [PubMed: 17105206]
25. Zeng Y, Caignan GA, Bunce RA, Rodriguez JC, Wilks A, Rivera M. J. Am. Chem. Soc 2005;127:9794–9807. [PubMed: 15998084]
26. Deshmukh R, Zeng Y, Furci LM, Huang H-w, Morgan BN, Sander S, Alontaga AY, Bunce RA, Moenne-Loccoz P, Rivera M, Wilks A. Biochemistry 2005;44:13713–13723. [PubMed: 16229461]
27. Unno M, Matsui T, Chu GC, Coutoure M, Yoshida T, Rousseau DL, Olson JS, Ikeda-Saito M. J. Biol. Chem 2004;279:21055–21061. [PubMed: 14966119]
28. Zeng Y, Deshmukh R, Caignan GA, Bunce RA, Rivera M, Wilks A. Biochemistry 2004;43:5222–5238. [PubMed: 15122888]
29. Friedman J, Lad L, Li H, Wilks A, Poulos TL. Biochemistry 2004;43:5239–5245. [PubMed: 15122889]
30. Caignan GA, Deshmukh R, Wilks A, Zeng Y, Huang H-W, Moenne-Loccoz P, Bunce RA, Eastman MA, Rivera M. J. Am. Chem. Soc 2002;124:14879–14892. [PubMed: 12475329]
31. Caignan GA, Deshmukh R, Zeng Y, Wilks A, Bunce RA, Rivera M. J. Am. Chem. Soc 2003;125:11842–11852. [PubMed: 14505406]
32. Rodriguez JC, Wilks A, Rivera M. Biochemistry 2006;45:4578–4592. [PubMed: 16584193]
33. Davydov RM, Yoshida T, Ikeda-Saito M, Hoffman BM. J. Am. Chem. Soc 1999;121:10656–10657.

34. Li Y, Syvitski RT, Chu GC, Ikeda-Saito M, La Mar GN. J. Biol. Chem 2003;279:6651–6663. [PubMed: 12480929]
35. Liu Y, Ma L-H, Zhang X, Yoshida T, Langry KC, Smith KM, La Mar GN. J. Am. Chem. Soc 2006;128:6391–6399. [PubMed: 16683803]
36. Koenigs Lightning L, Huang H-W, Moënne-Loccoz P, Loehr TM, Schuller DJ, Poulos TL, Ortiz de Montellano PR. J. Biol. Chem 2001;276:10612–10619. [PubMed: 11121422]
37. Fujii H, Zhang X, Tomita T, Ikeda-Saito M, Yoshida T. J. Am. Chem. Soc 2001;123:6475–6484. [PubMed: 11439033]
38. Matsui T, Furukawa M, Unno M, Tomita T, Ikeda-Saito M. J. Biol. Chem 2005;280:2981–2989. [PubMed: 15528205]
39. La Mar, GN.; Satterlee, JD.; de Ropp, JS. The Porphyrins Handbook, NMR of Hemoproteins, vol. 5. Kadish, KM.; Smith, KM.; Guilard, R., editors. San Diego: Academic Press; 2000. p. 185-298.
40. Sugishima M, Sakamoto H, Noguchi M, Fukuyama K. Biochemistry 2003;42:9898–9905. [PubMed: 12924938]
41. Sandström, J. Dynamic NMR Spectroscopy. New York: Academic Press; 1982.
42. Peyton DH. Biochem. Biophys. Res. Commun 1991;175:515–519. [PubMed: 2018499]
43. Yamamoto Y, Inoue Y, Suzuki T. Magn. Reson. Chem 1993;31:S8–S16.
44. Frankenberg-Dinkel N. Antoxidants Redox Signal 2004;6:825–834.
45. Zuiderweg ERP. Biochemistry 2000;43:5222–5238.
46. Bertini I, Luchinat C. Coord. Chem. Rev 1996;150:1–296.
47. Williams G, Clayden NJ, Moore GR, Williams RJP. J. Mol. Biol 1985;183:447–460. [PubMed: 2991533]
48. Emerson SD, La Mar GN. Biochemistry 1990;29:1556–1566. [PubMed: 2334714]
49. Johnston PD, Figueroa N, Redfield AG. Proc. Natl. Acad. Sci. USA 1979;76:3130–3134. [PubMed: 386331]
50. Piotto M, Sandek V, Sklenar V. J. Biomol. NMR 1992;2:661–666. [PubMed: 1490109]
51. Jeener J, Meier BH, Bachmann P, Ernst RR. J. Chem. Phys 1979;71:4546–4553.
52. Griesinger C, Otting G, Wüthrich K, Ernst RR. J. Am. Chem. Soc 1988;110:7870–7872.
53. Neal S, Nip AM, Zhang H, Wishart DS. J. Biomol. NMR 2003;26:215–240. [PubMed: 12766419]
54. Shrager RI. J. Assoc. Comput. Machin 1970;17:446–452.
55. Press, WH.; Flannery, BP.; Teukolsky, SA.; Vetterlin, WT. Numerical Recipes. Cambridge: Cambridge University Press; 1986.
56. Xia Z, Nguyen BD, Brunori M, Cutruzzola F, La Mar GN. Biophys. J 2005;89:4149–4158. [PubMed: 16150970]
57. Wüthrich, K. NMR of Proteins and Nucleic Acids. New York: Wiley & Sons; 1986.
58. Rodriguez JC, Zeng Y, Wilks A, Rivera M. J. Am. Chem. Soc 2007:11730–11742. [PubMed: 17764179]
59. Englander SW, Kallenbach NR. Quart. Rev. Biophys 1984;16:521–655.

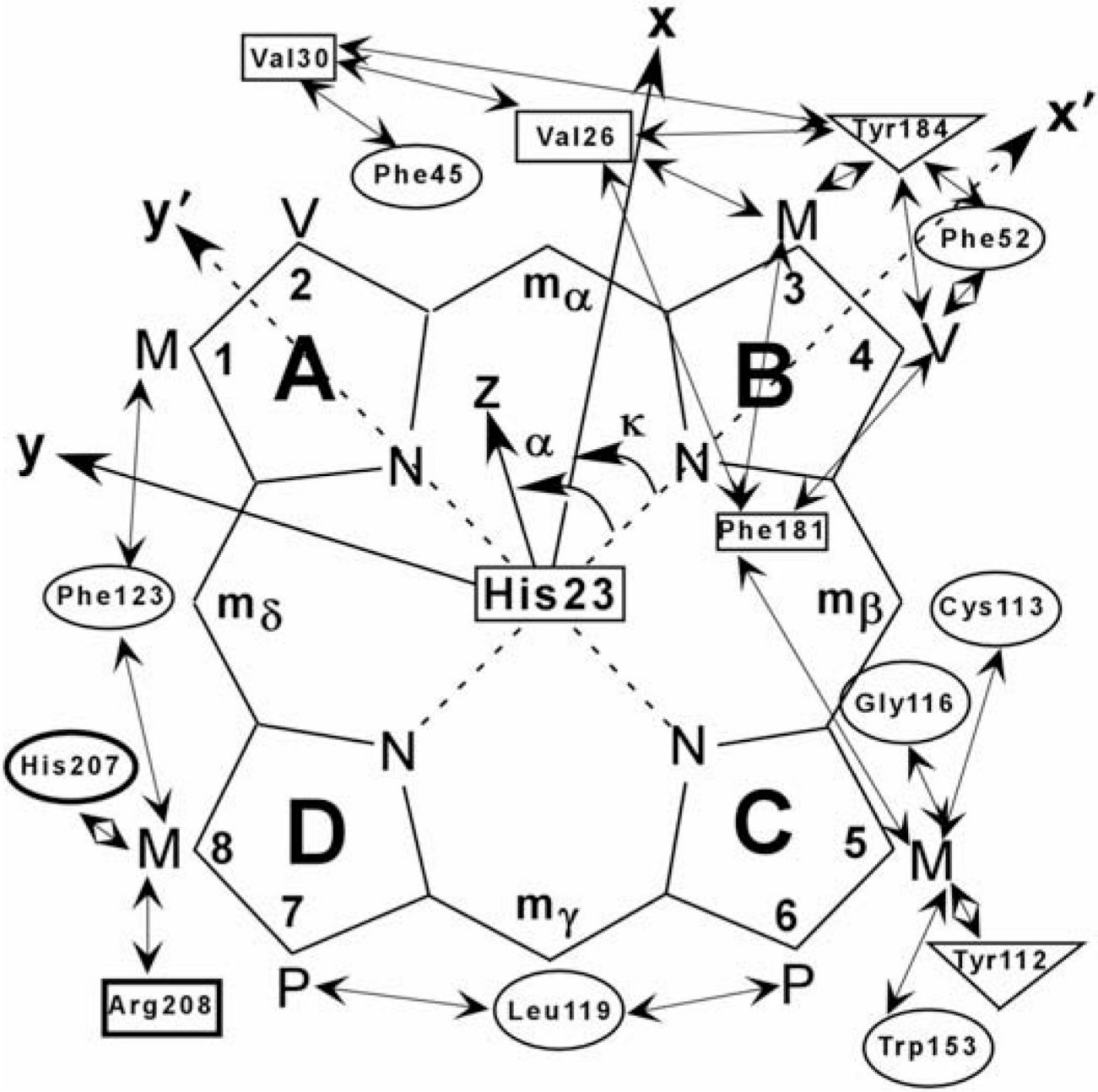

Fig. 1.

Schematic of the protohemin (PH) and the paramagnetically influenced proximal (squares) distal (circles) and equatorial (triangles) residues that are predicted to be, and observed, in contact with the heme or each other. The orientation of the axial His23 imidazole plane is shown as a rectangle. Also shown are the reference x', y', z', and the magnetic coordinate systems, x, y, z. The Euler rotation, $\Gamma(\alpha,\beta,\gamma)$, relates the two coordinate systems, $[x, y, z] = \Gamma(\alpha,\beta,\gamma)[x',y', z']$, where β is the tilt of the major magnetic axis, z, from the heme normal (z' axis), α is the direction of the tilt of the major magnetic axes as given by the angle between the projection of z' on the x, y plane and the x' axis; and $\kappa \sim \alpha + \gamma$ is the angle between the projection of the x axis on the x', y' plane and the x' axis.

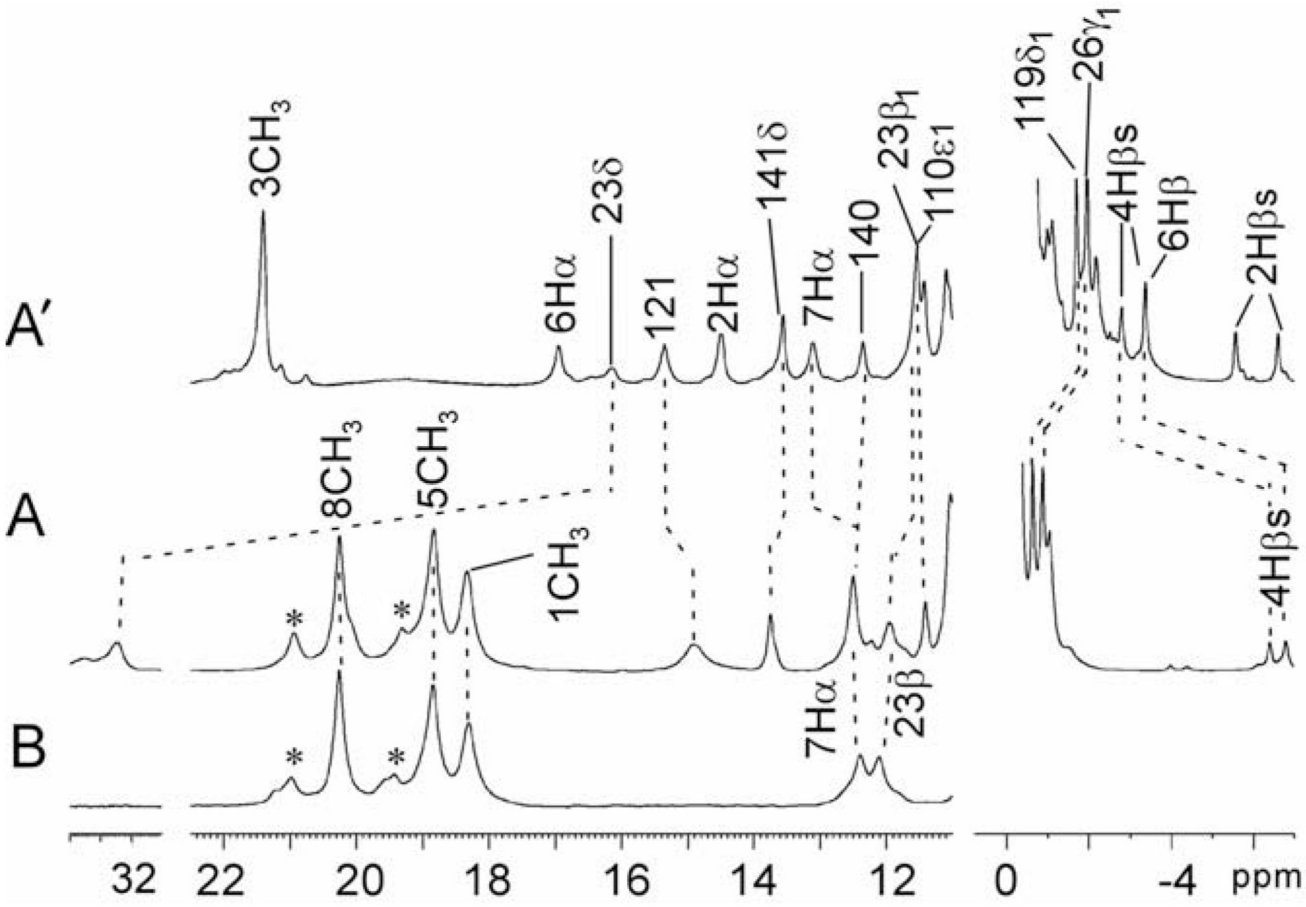

Fig. 2.

Resolved portions of the 600 MHz ^{1}H NMR spectra of WT (species A) *Nm*HO–PH–N_3, 50 mM phosphate, pH 7.1 at 25 °C in: (A) $^{1}H_2O$ and (B) $^{2}H_2O$; the same portions of the spectrum for the previously characterized *Nm*HO–PH–CN complex [20] are shown in (A′). Heme peaks are labeled in the Fischer notation and peaks from active site residues assigned by 2D NMR are labeled by residue number and position, and only by resonance number for peptide NHs.

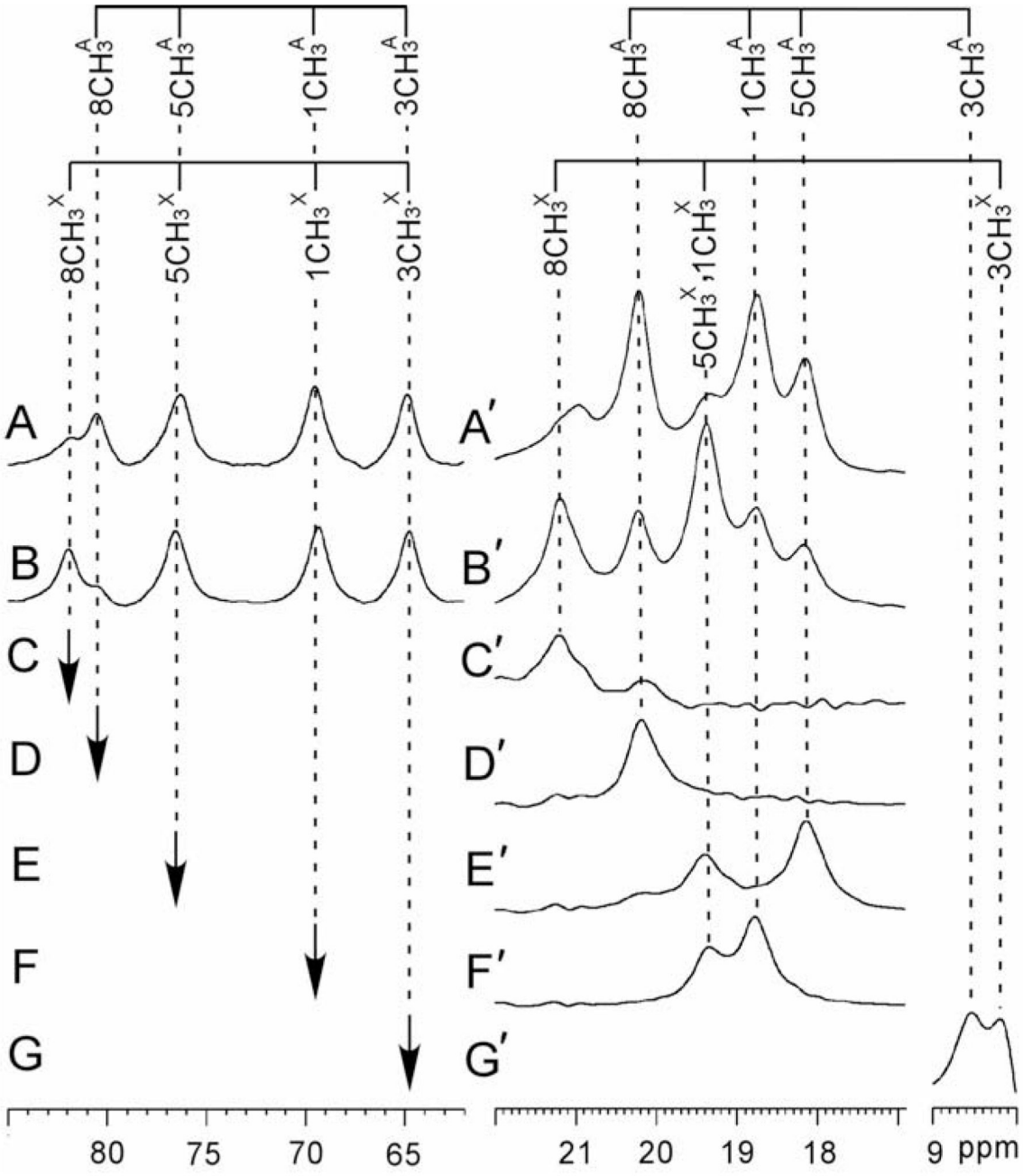

Fig. 3.

The heme methyl spectral window for the high-spin *Nm*HO–PH–H_2O complexes (with methyl peak labeled $i\mathrm{CH}_3^{\mathrm{A}}$ for the initial, native complex and $i\mathrm{CH}_3^{\mathrm{X}}$ for the "aged" or cleaved complex, as described previously [22]) at two different times (A, B), and for the low-spin *Nm*HO–PH–N_3 complex (methyl peak $i\mathrm{CH}_3^{\mathrm{A}}$ for the initial, native complex and $i\mathrm{CH}_3^{\mathrm{X}}$ for the "aged" complex) at the same two times (A′, B′), both at 25 °C, 50 mM phosphate and pH 7.1. (C–G) correspond to the sequential saturation of peaks $8\mathrm{CH}_3^{\mathrm{X}}, 8\mathrm{CH}_3^{\mathrm{A}}$, $(5\mathrm{CH}_3^{\mathrm{A}}, 5\mathrm{CH}_3^{\mathrm{X}})$, $(1\mathrm{CH}_3^{\mathrm{A}}, 1\mathrm{CH}_3^{\mathrm{X}})$ and $(3\mathrm{CH}_3^{\mathrm{A}}, 3\mathrm{CH}_3^{\mathrm{X}})$of the *Nm*HO–PH–$H_2O$

complexes as indicated by vertical arrows; and (C′–G′) correspond to the difference spectra for these same resonances in the *Nm*HO–PH–N_3 complexes, respectively.

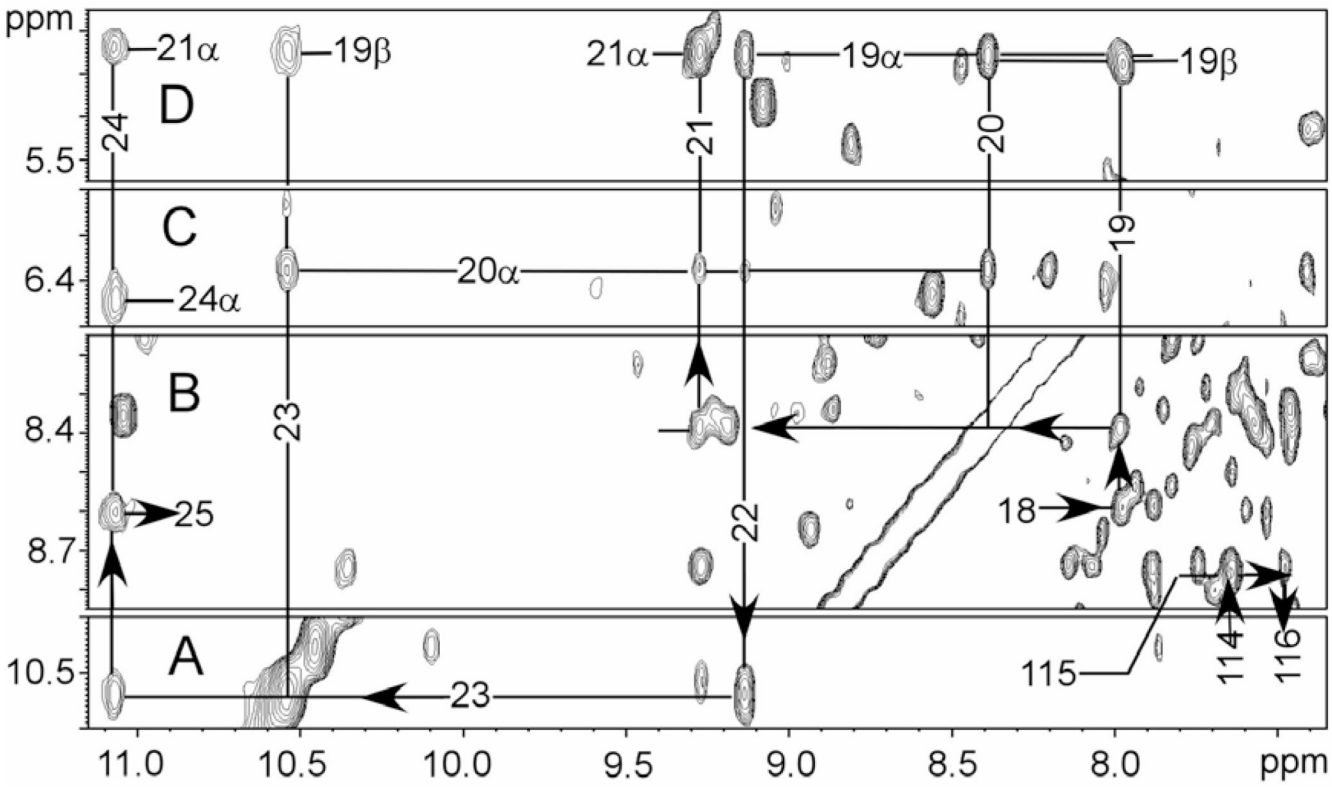

Fig. 4.

Portions of the 600 MHz ^{1}H NMR NOESY spectrum of *Nm*HO–PH–N_3 in $^{1}H_2O$, 50 mM in phosphate, pH 7.1 at 25 °C, illustrating the α-helical (A, B) $N_i - N_{i+1}$, (arrows) and some α_i-N_{i+1} (C, D) contacts for the hyperfine shifted residues Asp18-Val26, of the proximal helix and the $N_i - N_{i+1}$ contacts for the hyperfine shifted portion of Ala114-Gly116 of the distal helix (B). Residues are labeled as described in Fig. 3 and Fig 4.

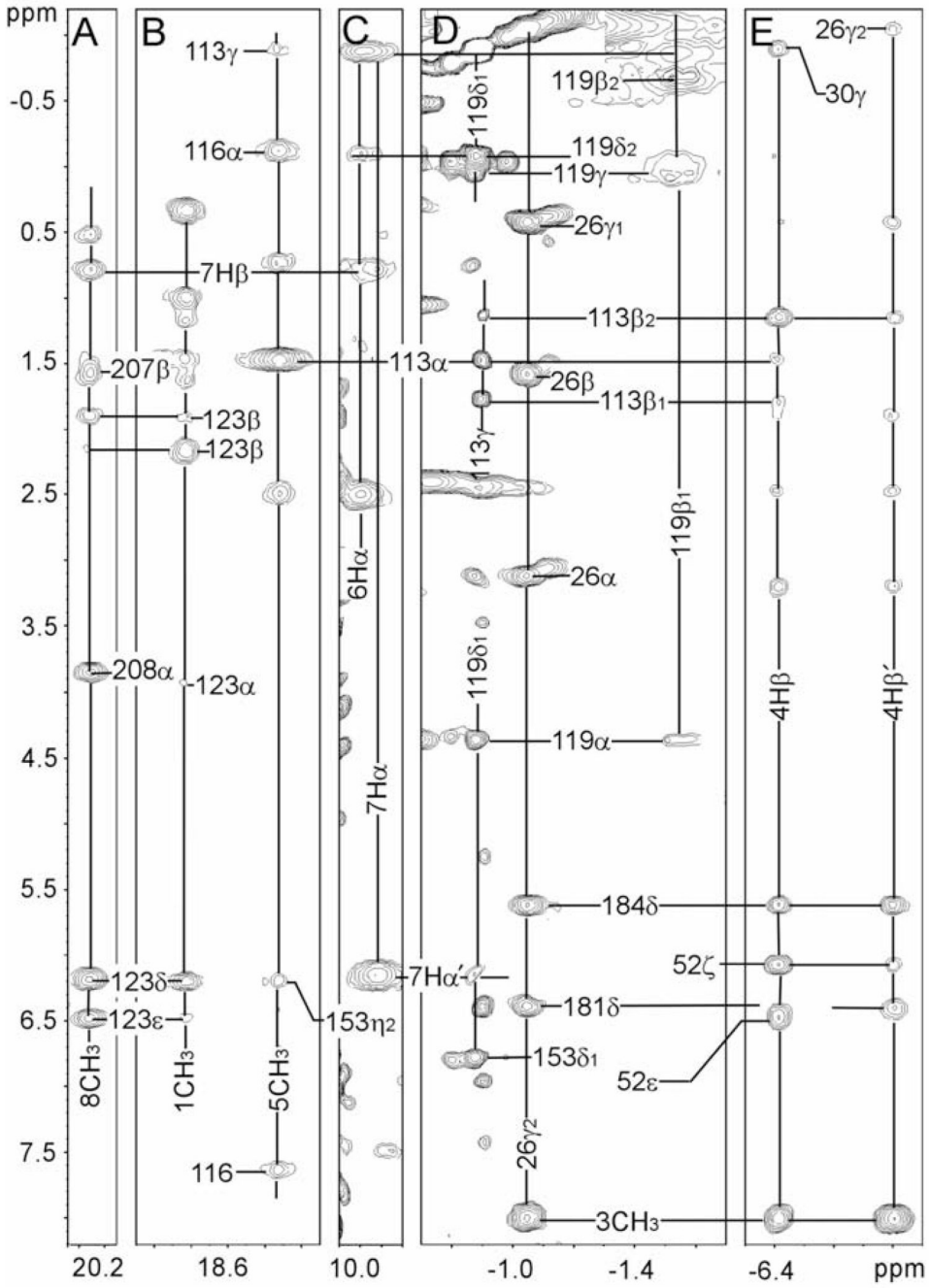

Fig. 5.

Portions of the 600 MHz ^{1}H NMR NOESY spectrum (mixing time 40 ms, repetition rate 2 s^{-1}) of *Nm*HO–PH–N_3 in $^{1}H_2O$, 50 mM in phosphate, pH 7.1 at 25 °C, illustrating the key heme contacts and interactions among such paramagnetically influenced active site residues, (A) $8CH_3$; (B) $1CH_3$ and $5CH_3$; (C) $6H_\alpha$ and $7H_\alpha$; (D) $3CH_3$ as well as key intra-residue contacts, and (D) $4H_\beta$s. The peak marked 208α and 207β in (A) are abolished in the “aged” or cleaved complex.

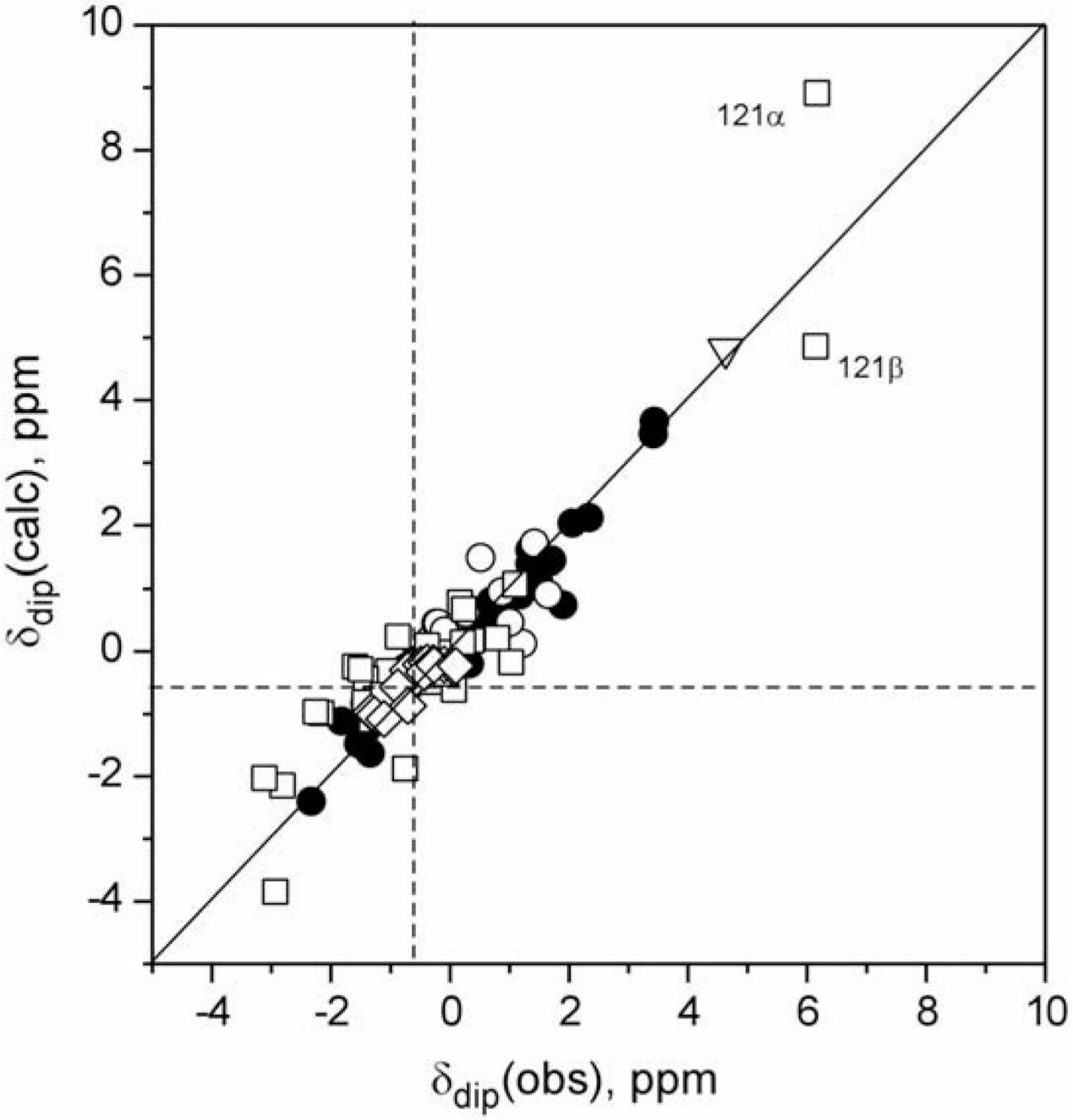

Fig. 6.

Plot of δ_{dip}(obs) versus δ_{dip}(calc) for the optimized anisotropy and orientation of χ for *Nm*HO–PH–N_3, with $\Delta\chi_{ax} = 2.3 \pm 0.1 \times 10^{-8}$ m^3/mol, $\Delta\chi_{rh} = -0.1 \pm 0.1 \times 10^{-8}$ m^3/mol, $\alpha = 240 \pm 20°$, $\beta = 5 \pm 1°$ and $\kappa = 140 \pm 30°$. The input data (proximal helix only) are shown in closed circles, the other, non-input data for the distal helix (open squares), the loop His137-Leu142 (open circles), and the helical fragment Ala180-Val187 (open diamonds). Points that deviate significantly from the ideal fit, which is represented by the solid line of unit slope, are labeled by residue number and position.

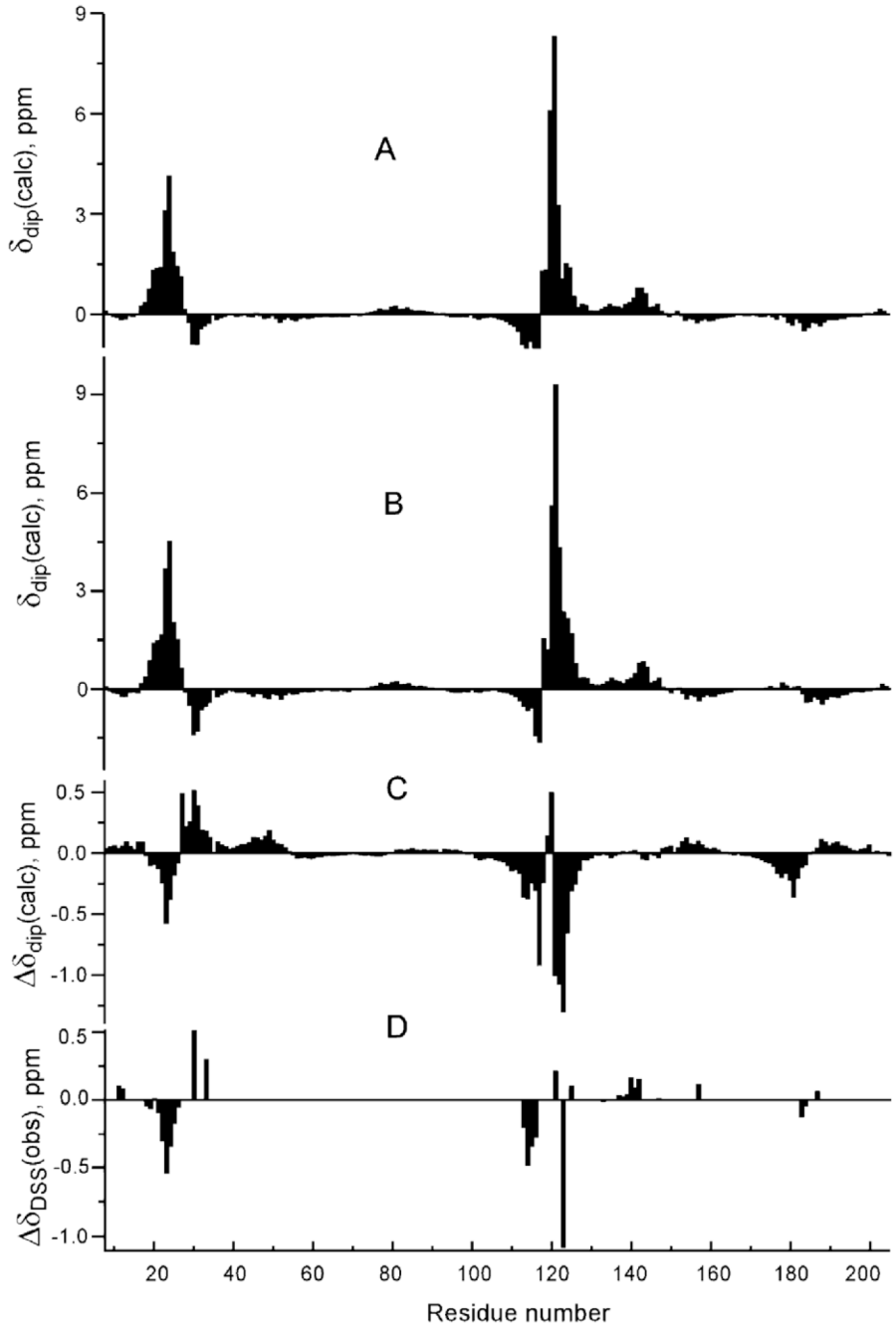

Fig. 7.

Plot of chemical shift data, in ppm, for peptide NHs versus residue number for *Nm*HO–PH–N_3 and *Nm*HO–PH–CN in ^1H_2O, 50 mM phosphate, pH 7.0 and 25 °C; (A) δ_{dip}(calc; *Nm*HO–PH–N_3), as determined in Fig. 6; (B) δ_{dip}(calc: *Nm*HO–PH–CN) as reported previously, [20] (C) $\Delta\delta_{dip}$(calc) = δ_{dip}(calc: *Nm*HO–PH–N_3) − δ_{dip}(calc: *Nm*HO–PH–CN); Eq. (4) for data shown in A and B, respectively; (D) $\Delta\delta_{DSS}$(obs) = δ_{DSS}(obs:*Nm*HO–PH–N_3) − δ_{DSS}(obs:*Nm*HO–PH–CN); Eq. (5), for assigned peptide NHs.

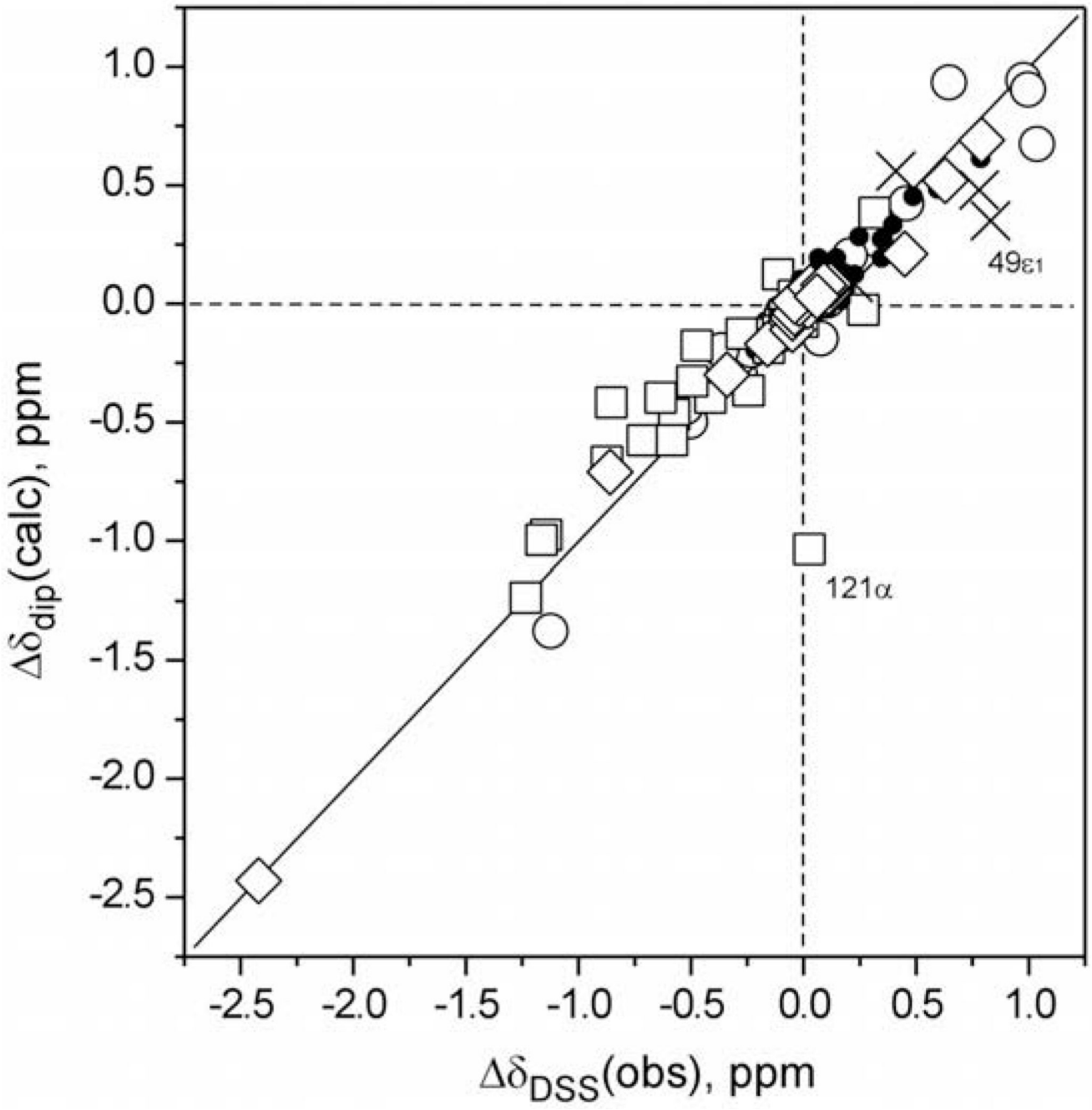

Fig. 8.

Plot of $\Delta\delta_{DSS}$(obs) (δ_{DSS}(obs; *Nm*HO–PH–N_3) − δ_{DSS}(obs; *Nm*HO–PH–CN)); Eq. (4)) versus $\Delta\delta_{dip}$(calc) (δ_{dip}(calc; *Nm*HO–PH–N_3) − δ_{dip}(calc; *Nm*HO–PH–CN)); Eq. (5)), for non-labile protons of non-ligated residues, with δ_{dip}(calc) obtained for the optimized magnetism for *Nm*HO–PH–N_3 (described in Fig. 6) and for *Nm*HO–PH–CN, as reported [20] previously. Data, are shown for the proximal helix (open circles), distal helix (open squares), fragment His137-Leu142 (closed circles), fragment Ala180-Val187 (open diamonds). Side chain labile protons are also included as *x*. Points that deviate significantly from the ideal fit, which is represented by a solid line of unit slope, are labeled by residue number and positions.

Table 1

Chemical shift data for assigned residues in *Nm*HO–PH–X[a]

		X = N_3^-		X = CN^-	Shift differences	
		δ_{DSS}(obs)[b]	δ_{dip}(calc)[c]	δ_{DSS}(obs)[d]	$\Delta\delta_{DSS}$(obs)[e]	$\Delta\delta_{dip}$(calc)[f]
Ala12	NH	9.04	−0.16	8.96	0.08	0.05
	$C_\alpha H$	3.38	−0.26	3.30	0.08	0.06
	$C_\beta H_3$	1.17	−0.29	1.02	0.15	0.11
Leu15	$C_\gamma H$	0.54	−0.12	0.57	−0.03	−0.03
	$C_{\delta1} H_3$	−0.65	−0.28	−0.65	0.00	−0.03
	$C_{\delta2} H_3$	0.11	−0.14	0.21	−0.10	−0.10
Asp18	NH	8.60	0.34	8.64	−0.04	−0.02
	$C_\alpha H$	4.91	0.43	4.97	−0.06	−0.05
	$C_{\beta1} H$	2.87	0.29	2.95	−0.08	−0.09
	$C_{\beta2} H$	2.78	0.26	2.85	−0.07	−0.03
Thr19	NH	7.98	0.75	8.04	−0.06	−0.10
	$C_\alpha H$	5.28	0.93	5.52	−0.24	−0.20
	$C_\beta H$	5.23	1.03	5.75	−0.52	−0.50
	$C_\gamma H_3$	1.41	0.43	1.70	−0.29	−0.20
	$O_\eta H$	5.60	0.36	5.90	−0.28	−0.30
Thr20	NH	8.38	1.30	8.37	0.01	−0.09
	$C_\alpha H$	6.38	3.45	6.30	0.08	−0.15
	$C_\beta H$	5.25	1.37	5.14	0.11	0.01
	$C_\gamma H_3$	2.41	2.11	2.27	0.14	0.10
Ala21	NH	9.27	1.36	9.36	−0.09	−0.12
	$C_\alpha H$	5.23	1.43	5.31	−0.08	−0.11
	$C_\beta H_3$	1.97	0.89	2.04	−0.07	−0.09
Val22	NH	9.14	1.40	9.44	−0.30	−0.24
	$C_\alpha H$	4.60	1.11	4.87	−0.27	−0.21
	$C_\beta H$	2.44	0.79	2.72	−0.28	−0.23

		X = N_3^-		X = CN^-	Shift differences	
		δ_{DSS}(obs)[b]	δ_{dip}(calc)[c]	δ_{DSS}(obs)[d]	$\Delta\delta_{DSS}$(obs)[e]	$\Delta\delta_{dip}$(calc)[f]
	$C_{\gamma 1}H_3$	1.04	1.15	1.56	−0.52	−0.44
	$C_{\gamma 2}H_3$	1.17	0.60	1.40	−0.23	−0.20
His23	NH	10.54	3.10	11.08	−0.54	−0.57
	$C_\alpha H$	6.25	4.82	7.37	−1.12	−1.38
	$C_{\beta 1}H$	12.50		11.53	[g]	
	$C_{\beta 2}H$	9.54		10.75	[g]	
Asp24	NH	11.07	4.13	11.41	−0.34	−0.27
	$C_\alpha H$	6.44	3.65	6.80	−0.36	−0.20
	$C_{\beta 1}H$	3.52	1.59	3.65	−0.13	−0.10
	$C_{\beta 2}H$	4.14	2.02	4.30	−0.16	−0.13
Ser25	NH	8.60	1.85	8.77	−0.17	−0.17
Val26	NH	8.28	1.42	8.33	−0.05	−0.08
	$C_\alpha H$	3.12	−0.27	2.80	0.32	0.27
	$C_\beta H$	1.57	0.64	1.60	−0.03	0.05
	$C_{\gamma 1}H_3$	−0.98	−2.41	−1.96	0.98	0.94
	$C_{\gamma 2}H_3$	0.43	−0.09	0.51	−0.08	−0.13

[a] In ^1H_2O 50 mM in phosphate, pH 7.1 at 25 °C.

[b] Chemical shifts, in ppm, referenced to DSS via the solvent resonance.

[c] Dipolar shift, in ppm, at 25 °C for *Nm*HO–PH–N_3, calculated by the optimized orientation and anisotropies of the paramagnetic susceptibility tensor as described in Fig. 6.

[d] Chemical shift, in ppm, referenced to DSS, as reported previously [20].

[e] $\Delta\delta_{DSS}$(obs), as described in Eq. (5).

[f] $\Delta\delta_{dip}$(calc), as described in Eq. (4).

[g] Possesses large contribution from contact shifts.